

On the coupling between barotropic and baroclinic modes of extratropical atmospheric variability

Article

Accepted Version

Boljka, L., Shepherd, T. G. ORCID: <https://orcid.org/0000-0002-6631-9968> and Blackburn, M. (2018) On the coupling between barotropic and baroclinic modes of extratropical atmospheric variability. *Journal of the Atmospheric Sciences*, 75 (6). pp. 1853-1871. ISSN 1520-0469 doi: 10.1175/JAS-D-17-0370.1 Available at <https://centaur.reading.ac.uk/75911/>

It is advisable to refer to the publisher's version if you intend to cite from the work. See [Guidance on citing](#).

To link to this article DOI: <http://dx.doi.org/10.1175/JAS-D-17-0370.1>

Publisher: American Meteorological Society

All outputs in CentAUR are protected by Intellectual Property Rights law, including copyright law. Copyright and IPR is retained by the creators or other copyright holders. Terms and conditions for use of this material are defined in the [End User Agreement](#).

www.reading.ac.uk/centaur

CentAUR

Central Archive at the University of Reading

Reading's research outputs online

On the coupling between barotropic and baroclinic modes of extratropical atmospheric variability

3 Lina Boljka* and Theodore G. Shepherd

⁴ *Department of Meteorology, University of Reading, Reading, United Kingdom*

5 Michael Blackburn

⁶ *National Centre for Atmospheric Science, University of Reading, Reading, United Kingdom*

⁷ **Corresponding author address:* Lina Boljka, Department of Meteorology, University of Reading,

⁸ P.O. Box 243, Reading, RG6 6BB, United Kingdom.

⁹ E-mail: l.boljka@pgr.reading.ac.uk

ABSTRACT

10 The baroclinic and barotropic components of atmospheric dynamics are usu-
11 ally viewed as interlinked through the baroclinic life cycle, with baroclinic
12 growth of eddies connected to heat fluxes, barotropic decay connected to mo-
13 mentum fluxes, and the two eddy fluxes connected through the Eliassen-Palm
14 wave activity. However, recent observational studies have suggested that these
15 two components of the dynamics are largely decoupled in their variability,
16 with variations in the zonal mean flow associated mainly with the momen-
17 tum fluxes, variations in the baroclinic wave activity associated mainly with
18 the heat fluxes, and essentially no correlation between the two. These rela-
19 tionships are examined in a dry dynamical core model under different con-
20 figurations and in Southern Hemisphere observations, considering different
21 frequency bands to account for the different timescales of atmospheric vari-
22 ability. It is shown that at intermediate periods longer than 10 days the decou-
23 pling of the baroclinic and barotropic modes of variability can indeed occur as
24 the eddy kinetic energy at those time scales is only affected by the heat fluxes
25 and not the momentum fluxes. The baroclinic variability includes the oscil-
26 lator model with periods of 20-30 days. At both the synoptic timescale and
27 the quasi-steady limit the baroclinic and barotropic modes of variability are
28 linked, consistent with baroclinic life cycles and the positive baroclinic feed-
29 back mechanism, respectively. In the quasi-steady limit the pulsating modes
30 of variability and their correlations depend sensitively on the model climatol-
31 ogy.

32 1. Introduction

33 The midlatitude dynamics of the Southern Hemisphere (SH) exhibit two distinct so-called annu-
34 lar modes of variability: the Southern Annular Mode (SAM) (e.g. Kidson 1988; Hartmann and Lo
35 1998) and the Baroclinic Annular Mode (BAM) (Thompson and Woodworth 2014). The former
36 is based on empirical orthogonal function (EOF) analysis of zonal mean zonal wind and repre-
37 sents north-south shifts of the jet stream, which are mainly driven by corresponding shifts in eddy
38 momentum fluxes (e.g. Hartmann and Lo 1998; Lorenz and Hartmann 2001). The latter is based
39 on EOF analysis of eddy kinetic energy (EKE) and represents amplitude variations of this field,
40 which are mainly driven by corresponding variations in eddy heat fluxes (Thompson and Wood-
41 worth 2014). The SAM has an equivalent barotropic vertical structure and is often referred to as a
42 barotropic mode of variability, whereas the BAM has a stronger vertical structure, as well as being
43 directly linked to heat fluxes, and is therefore related to variability in baroclinic processes.

44 Thompson and Woodworth (2014) found that the SAM was essentially uncorrelated with eddy
45 heat fluxes, the BAM was essentially uncorrelated with eddy momentum fluxes, and there was only
46 a small (negligible) correlation between the SAM and BAM. These findings led to the conclusion
47 that the eddy momentum and heat fluxes are somewhat independent, hence there is a decoupling
48 between baroclinic and barotropic modes of variability. This was a somewhat counterintuitive re-
49 sult as the momentum and heat fluxes (and also baroclinic and barotropic processes) are usually
50 viewed as linked through eddy growth and decay in the Eliassen-Palm (EP) wave activity perspec-
51 tive (e.g. Simmons and Hoskins 1978; Edmon et al. 1980), and both Robinson (2000) and Lorenz
52 and Hartmann (2001) identified a baroclinic feedback associated with annular mode anomalies.

53 However, it is perfectly conceivable to have barotropic variability with fixed baroclinic wave
54 sources (e.g. Vallis et al. 2004). In particular, different momentum fluxes can arise from the same

55 heat fluxes, depending on the upper-tropospheric conditions, as in LC1 (equatorward wave break-
56 ing) and LC2 (poleward wave breaking) life-cycle experiments (Thorncroft et al. 1993). Moreover,
57 Pfeffer (1987, 1992) argued that typical aspect ratios implied that heat fluxes mainly act to drive
58 the residual circulation, whereas momentum fluxes mainly drive the zonal mean flow tendency,
59 implying irrelevance of heat fluxes for the zonal mean flow. This argument has been formalised
60 in a companion study (Boljka and Shepherd 2018), which, using multiscale asymptotic methods,
61 showed that under such conditions and under synoptic temporal and spatial scale averaging, wave
62 activity (generalised eddy kinetic energy) and the vertical component of EP flux (related to heat
63 flux) are indeed related on timescales longer than synoptic, and that momentum fluxes do not
64 directly affect this coupling on such timescales.

65 Thompson and Barnes (2014) further found an oscillator model between EKE and heat flux with
66 a timescale of 20-30 days, which was reflected in the BAM mode. This model has no influence
67 from the momentum fluxes and is purely baroclinic by nature with a relationship with baroclinicity
68 (vertical wind shear). A similar oscillator model was also found for the Northern Hemisphere in
69 Ambaum and Novak (2014). Such an oscillating relationship is consistent with weakly nonlinear
70 models of baroclinic instability, such as in Pedlosky (1970).

71 Wang and Nakamura (2015, 2016) also pointed out a relationship between wave activity and
72 heat flux with a similar timescale as in Thompson and Barnes (2014), but only for the South-
73 ern Hemisphere (SH) summer. This suggests that not all seasons exhibit the oscillating behavior
74 (between EKE and heat flux). Wang and Nakamura (2015) further pointed out that momentum
75 and heat fluxes primarily act at different timescales: heat fluxes act primarily at about 20 to 30
76 day periods, whereas momentum fluxes act at shorter periods. Wang and Nakamura (2016) in-
77 vestigated the relationship between wave activity and heat fluxes and found that the meridionally

78 confined baroclinic zone in SH summer provides a wave guide that lets different modes interfere
79 and produce larger amplitude heat fluxes with a 20-30 day periodicity.

80 Here we look into the behavior discussed above using different configurations of a simplified
81 model and the ERA-Interim reanalysis (described in section 2a). The different model config-
82 urations are not intended to realistically mimic the real atmosphere but rather to examine the
83 baroclinic-barotropic coupling across a wide range of dynamical regimes. They also facilitate
84 comparison to previous work done on the baroclinic and barotropic modes of variability using
85 simplified models (e.g. Sparrow et al. 2009; Sheshadri and Plumb 2017). The methods are given
86 in section 2, and the theoretical background in section 3. We first examine in detail one particular
87 (equinox) configuration of the model, in section 4, in order to understand the nature of baroclinic-
88 barotropic interactions on various timescales. In section 5 we assess the generality of our results
89 by comparing them with the winter and summer hemispheres of a solstice configuration of the
90 model, and use these findings to interpret the SH behavior seen in ERA-Interim. Conclusions are
91 given in section 6.

92 **2. Methods**

93 *a. Data*

94 The numerical model used for this study is the dry dynamical core version of the UK Met
95 Office Unified Model (UM) version 8.6 with ENDGame semi-Lagrangian dynamical core (Walters
96 et al. 2014). The model configuration follows Held and Suarez (1994) with some modifications,
97 being forced through Newtonian relaxation of the temperature field to a prescribed equilibrium
98 profile, with linear frictional and thermal damping. The model resolution used is N96L63 with a
99 model top at 32 km (1.875° in longitude, 1.25° in latitude and varying vertical resolution - from

100 approximately 200 m in the lower troposphere to approximately 1000 m in the stratosphere) and
101 is run for 10800 days, of which the first 1440 days are taken as a spin-up period. The output is
102 analysed at daily resolution and in height coordinates.

103 Two different model configurations were used for this study: (i) the usual Held-Suarez con-
104 figuration with perpetual equinox conditions as specified in Held and Suarez (1994), and (ii) a
105 stratospheric perpetual solstice configuration, following Polvani and Kushner (2002)’s strong po-
106 lar vortex forcing ($\gamma = 4$) with a troposphere to stratosphere transition at 200 hPa (as used in She-
107 shadri et al. 2015). Note that the tropospheric equilibrium temperature profile was not modified,
108 only the stratospheric profile. In this configuration the winter hemisphere (with a strong polar vor-
109 tex) is in the Southern Hemisphere (SH) and the summer hemisphere (with a warmer stratosphere)
110 is in the Northern Hemisphere (NH). There is no orography or other longitudinal asymmetries
111 (such as land-sea contrast) that would give rise to forced stationary planetary waves, and the lack
112 of a seasonal cycle or other sources of external variability means that the model simulations are
113 statistically stationary.

114 The different model configurations exhibit climatological jets at different latitudes and with
115 different strengths, and thereby give rise to different variability. We have three different model
116 climatologies to compare: equinox, winter and summer. The equinox configuration gives a strong
117 jet centred at 40° (Fig. S1a in supplementary material), whereas the winter and summer hemi-
118 spheres of the solstice configuration have weaker jets around 45° and 35° latitude (Fig. S1b,c in
119 supplementary material), respectively.

120 In order to test the relationships found in the simplified model in a more realistic setting, the
121 model data are compared to the ERA-Interim observational reanalysis dataset from the European
122 Centre for Medium-Range Weather Forecasts (Dee et al. 2011). The data are analysed as daily
123 mean (from four times daily resolution – the eddy fluxes are first computed at 6-hourly resolution

and then averaged over 24 h) for the time period between 1 January 1981 and 31 December 2010 (10957 days) on a grid with a resolution of 0.7° in latitude and longitude, and 27 pressure levels between 1000 hPa and 100 hPa. The temporal anomalies were formed by removing the seasonal cycle (subtracting the climatology of each calendar day), hence no specific season is analysed. Only Southern Hemisphere observed data were analysed in this study, where the climatological jet is centred around 50° latitude (Fig. S1d in supplementary material).

b. EOF and regression analysis

Empirical orthogonal function (EOF) analysis is adopted to obtain the leading modes of variability of various fields. The EOF of zonal mean zonal wind ($[u]$) is called SAM (after Southern Annular Mode), where the dipolar mode (representing shifting of the jet) is called SAM1 (usually the leading mode of variability) and the tripolar mode (representing sharpening and strengthening of the jet) is called SAM2 (usually the second mode of variability). The EOF of eddy kinetic energy ($EKE = 0.5 [u^{*2} + v^{*2}]$) is called BAM (after Baroclinic Annular Mode found in Thompson and Woodworth 2014), where BAM1 represents the monopolar mode (representing amplitude variations in the EKE field), BAM2 the dipolar mode (representing latitudinal shifts of the field) and BAM3 the tripolar mode (representing sharpening and strengthening of the field). Here the square brackets ($[.]$) represent the zonal mean, the asterisk (*) represents perturbations from the zonal mean, u is zonal velocity and v is meridional velocity. We recognize that the different EOFs are statistical rather than physically distinct entities, so are used only as a basis for our analysis which focuses on the coupling between barotropic and baroclinic components of the variability.

Additional modes of variability are defined based on eddy momentum ($[v^*u^*]$) and heat ($[v^*\theta^*]$) fluxes, called EMF and EHF, respectively, where θ is potential temperature. Here EMF1 and EHF1 are monopolar modes (representing amplitude variations), EMF2 and EHF2 are dipolar

147 modes (representing latitudinal shifts) and EHF3 is a tripolar mode (representing sharpening and
 148 strengthening of the field). Note that the modes are numbered according to their spatial structure
 149 and not by the variance explained, hence in some cases the leading modes can be SAM2, BAM2
 150 etc. (as shown in Table 1).

151 Before calculating the EOFs of the fields, a mass weighted vertical average is applied to the
 152 zonal mean model fields in height coordinates:

$$\langle T \rangle = \frac{\sum_{k=0}^N [\rho T]_k (z_{k+1/2} - z_{k-1/2})}{\sum_{k=0}^N [\rho]_k (z_{k+1/2} - z_{k-1/2})} \quad (1)$$

153 where T is the zonally averaged field of interest, ρ is density, $\langle \cdot \rangle$ is vertical average, k represents
 154 the vertical levels of the given quantity, $k \pm 1/2$ represents the half levels (vertical levels between
 155 k levels), N is the top vertical level of interest and z is the vertical coordinate. For ERA-Interim
 156 a pressure weighted vertical average is applied: $\langle T \rangle = p_o^{-1} \sum_{k=0}^N [T]_k (p_{k+1/2} - p_{k-1/2})$ where p is
 157 pressure and $p_o = \sum_{k=0}^N (p_{k+1/2} - p_{k-1/2})$. The vertical average is taken from the surface up to
 158 11.5km (200 hPa for ERA-Interim), except for heat flux where 5 km (500 hPa for ERA-Interim)
 159 was used since θ increases rapidly with height. Thus only tropospheric variability is represented in
 160 these diagnostics. These vertically averaged fields, weighted by $\sqrt{\cos \phi}$, are then used to calculate
 161 EOFs of zonal mean zonal wind, EKE, eddy heat and eddy momentum flux.

162 After calculating the EOFs, various fields are regressed onto the principal components (PC) of
 163 these modes of variability. The regressed fields include zonal mean zonal wind, EKE, eddy heat
 164 and eddy momentum flux. These show the relationship between the different dynamical fields
 165 involved in each mode of variability as well as identify the leading modes of variability in terms of
 166 their spatial structure. The correlations between different PC timeseries of SAM and BAM modes
 167 of variability are given in Tables 2-4, and are discussed later, in context.

For reference, the contours in Fig. 1 show regressions of zonal mean zonal wind on SAM1,2, of EKE on BAM1,2,3, of momentum flux on EMF1,2 and of heat flux on EHF1,2,3, for the model equinox configuration using unfiltered data and without any time lags. The colours in the figures show the climatologies of the regressed fields. The horizontal pairing of panels reflects the dominant relationships between modes (e.g. SAM1 has a clear relationship with EMF1 through the zonal momentum equation). The figure illustrates the typical spatial structures that these modes have, as described above.

c. Power spectrum, temporal filtering and cross-spectrum analysis

To calculate the power spectra of the PC timeseries of the EOF fields (e.g. SAM, BAM, EHF, EMF), we follow the methodology used in Byrne et al. (2016). The data are first windowed using a Hanning window, then a periodogram is calculated and finally the fields are smoothed using Daniell filters following Bloomfield (2000).

These power spectra (based on unfiltered data) were used to determine the frequency bands at which different dynamical processes take place (section 4). The original data (not PC timeseries) were then filtered according to the frequency bands using the Lanczos filter (Duchon 1979) and EOFs were re-calculated from the filtered data. Note that the EKE, heat flux and momentum flux time series are filtered, not each component of them separately (e.g. u , v , θ) as we are interested in the wave-mean flow interaction on different timescales, rather than in which waves (low or high frequency) contribute to the behavior.

The cross-spectrum analysis was computed following Lorenz and Hartmann (2001). We first obtained the relevant unfiltered timeseries (section 3), then we divided them into 256 or 512-day sections (for comparison) overlapped by 128 or 256 days, respectively, and windowed each section by a Hanning window. These gave at least 72 or 36 degrees of freedom, respectively. The cross-

191 spectra of each section were then averaged and smoothed using Daniell filters (as for the power
192 spectra).

193 3. Theoretical background

194 Wave-mean flow interactions are usually studied using the zonal momentum budget and
195 Eliassen-Palm (EP) wave activity theory, and the Transformed Eulerian Mean (TEM) perspec-
196 tive (Andrews and McIntyre 1976) yields a direct link between the two quantities. However, the
197 BAM modes are based on EKE. Whilst EKE may be considered a proxy for EP wave activity, there
198 is also an EKE equation derivable within the TEM framework, which in log-pressure coordinates
199 is (Plumb 1983)

$$\frac{\partial[K_E]}{\partial t} = C(P_E \rightarrow K_E) - C(K_E \rightarrow K_M) - \frac{1}{p_{ln}} \nabla \cdot \mathbf{B}(K_E) + S(K_E) \quad (2)$$

200 where

$$C(P_E \rightarrow K_E) = \frac{R p_{ln}^\kappa [\mathbf{u}^* \theta^*] \cdot \nabla[\theta]}{H \frac{\partial[\theta]}{\partial z_{ln}}} \quad (3)$$

201 represents the conversion from eddy potential energy (P_E) to EKE (K_E), $C(K_E \rightarrow K_M) = p_{ln}^{-1} [u] \nabla \cdot$
202 \mathbf{F} represents the conversion from EKE (K_E) to zonal mean kinetic energy (K_M), $\mathbf{B}(K_E) = p_{ln} [\mathbf{u}^* \cdot$
203 $\phi^*] + [u] \mathbf{F}$ is the EKE flux term and $S(K_E) = [\mathbf{u}^* \cdot \mathbf{L}^*]$ is the source-sink term of EKE. Here

$$\mathbf{F} = p_{ln} \left(-[u^* v^*], \frac{f[v^* \theta^*]}{\partial[\theta]/\partial z_{ln}} \right)$$

204 is the quasi-geostrophic (QG) EP flux (its divergence represents the eddy torque on the mean flow),
205 $\nabla = (\partial/\partial y, \partial/\partial z_{ln})$, p_{ln} = pressure/1000 hPa, $z_{ln} = -H \ln p_{ln}$ is log-pressure vertical coordinate,
206 $\kappa = R/c_p$, R is gas constant, c_p is specific heat at constant pressure, y represents latitude, \mathbf{L} is
207 frictional force, ϕ is geopotential, $\mathbf{u} = (u, v, w)$ is velocity vector, H is a constant scale height
208 (approximately 10 km), and f is the Coriolis parameter.

209 *a. Simplified TEM equations*

210 Lorenz and Hartmann (2001) used cross-spectrum analysis to show that the vertically averaged
 211 zonal mean zonal wind ($z_u = \langle [u] \rangle$ with $\langle . \rangle$ as vertical average) and eddy momentum flux conver-
 212 gence ($m = -\partial_y (\langle \rho_o [u^* v^*] \rangle)$ with $\partial_y = \partial/\partial y$ and ρ_o vertical density profile) were linearly related
 213 according to

$$\frac{\partial z_u}{\partial t} = m - \frac{z_u}{\tau}, \quad (4)$$

214 with τ a constant. This relationship follows from the zonal momentum equation under QG scal-
 215 ing provided the source-sink term can be represented as a linear damping $-z_u/\tau$ (dominated by
 216 boundary layer friction). As discussed by Boljka and Shepherd (2018), the relationship between
 217 m and $\partial z_u/\partial t$ is only approximate, since planetary scale heat fluxes also contribute to angular
 218 momentum via meridional mass redistribution, but the latter are negligible in QG scaling (Haynes
 219 and Shepherd 1989). Applying a spectral analysis (Fourier Transform) yields a cross-spectrum
 220 relationship (Lorenz and Hartmann 2001)

$$\frac{\bar{Z}M}{\bar{Z}Z} = i\omega + \frac{1}{\tau} \quad (5)$$

221 where Z and M represent the Fourier transforms of z_u and m , respectively, the overbar denotes the
 222 complex conjugate, and ω is the angular frequency. τ is determined by finding an empirical linear
 223 regression to the cross spectrum (as described in Appendix A of Lorenz and Hartmann 2001)

$$\frac{\bar{Z}M}{\bar{Z}Z} = \beta + i\vartheta\omega,$$

224 from which $\tau = \vartheta/\beta$.

225 The relationship (5) suggests that the real part of the cross spectrum $\bar{Z}M/\bar{Z}Z$ is constant (τ^{-1}),
 226 while the imaginary part of the cross spectrum changes linearly with ω . This is illustrated in
 227 section 4.

Thompson and Woodworth (2014) and Thompson and Barnes (2014) suggested there existed a relationship between EKE and heat flux, independent of momentum flux convergence or zonal mean zonal wind. Thompson et al. (2017) hence suggested a relationship between EKE and heat flux that is similar to (4), namely

$$\frac{\partial [K_E]}{\partial t} = \alpha_{EKE} [v^* \theta^*] - \frac{[K_E]}{\tau_{EKE}} \quad (6)$$

where $|\alpha_{EKE}| \approx 3 \times 10^{-5} \text{ m K}^{-1} \text{ s}^{-2}$ and $\tau_{EKE} \approx 3 \text{ days}$ are constants, EKE is taken at 300 hPa, heat flux is taken at 850 hPa and both quantities were averaged meridionally between 40° and 60° latitude where EKE peaks (in ERA-Interim data). Thompson et al. (2017) found that such a simple model reproduced the oscillator model of Thompson and Barnes (2014), thus we test this relationship using cross-spectrum analysis to see how well it holds at different timescales. The cross-spectrum relationship corresponding to (6) is

$$\alpha_{EKE} \frac{\overline{EH}}{\overline{EE}} = i\omega + \frac{1}{\tau_{EKE}}, \quad (7)$$

where E and H now represent Fourier Transforms of EKE and heat flux, respectively. In contrast to (5), there is now an empirical factor, α_{EKE} (since (6) is not exact), which is determined by finding a linear regression to $\overline{EH}/\overline{EE}$ at frequencies lower than 0.1 cycles per day so that the imaginary part of $\alpha_{EKE} \overline{EH}/\overline{EE}$ is proportional to ω .

Equation (6) is simplified compared to the TEM EKE equation (2), only representing $C(P_E \rightarrow K_E)$ (3) explicitly (assuming $[w^* \theta^*] \propto [v^* \theta^*]$, which is valid under QG scaling), with the other terms subsumed in the linear damping term. Although latitudinal averaging will eliminate the EKE flux component of (2), it will not eliminate the $C(K_E \rightarrow K_M)$ term unless $[u]$ is slowly varying compared to $\nabla \cdot \mathbf{F}$, which is not the case. In this respect, the wave activity equation is much cleaner (Wang and Nakamura 2015, 2016). Our approach here is not to justify the approximation (6) but rather to examine how well it holds across timescales, as a way of understanding the observed

BAM-SAM decoupling. Based on the analysis of Boljka and Shepherd (2018) we expect that (in addition to latitudinal averaging) the relationship (6) would only hold at timescales longer than synoptic (and not necessarily at quasi-steady states), which is also tested below.

4. Equinox results

a. Cross-spectra

Lorenz and Hartmann (2001) have shown in observations that cross spectrum analysis (5) supports the relationship between vertically averaged zonal mean zonal flow and eddy momentum flux convergence described by (4). Indeed, Fig. 2a shows that these two quantities are related in the equinox model configuration at all frequencies as the real part of the cross spectrum is constant and proportional to τ^{-1} with $\tau \approx 10.6$ days, and the imaginary part of the cross spectrum nicely follows the ω slope. Fig. 2b shows that the phase difference between m and z_u at low frequencies is small (they are in phase), whereas at the highest frequencies, corresponding to synoptic timescales of 5-10 days, they are nearly 90° out of phase. These two figures thus clearly illustrate that at very low frequencies $z_u/\tau \approx m$ whereas at the highest frequencies $\partial z_u/\partial t \approx m$, as expected from (4).

In section 3 we presented a simplified theory for the EKE budget (6,7), which is analogous to Lorenz and Hartmann (2001)'s approximation for the zonal momentum equation (4,5). Here we test this theory using cross spectrum analysis (7) after averaging over different latitudinal bands.

First, we test the relationship for a 20-degree latitudinal band (EKE taken at 9000 m, heat flux at 1500 m, and both averaged between 30° and 50° latitude where both quantities peak, Fig. 1e-j in colours) for the equinox model configuration, using different lengths of segments: 256 and 512 (Fig. 3). In general, for both lengths of segments the relationship holds well at frequencies lower

271 than 0.1 cycles per day, above which the imaginary part of the cross spectrum becomes constant
 272 with frequency or even decreases, while the real part of the cross spectrum remains reasonably
 273 constant. Different segment lengths show that the peaks apparent at synoptic timescales are rea-
 274 sonably random and that noise increases as longer segments are taken due to fewer degrees of
 275 freedom and finer frequency resolution. $|\alpha_{EKE}|$ varies between 7 and $8.5 \times 10^{-5} \text{ m K}^{-1} \text{ s}^{-2}$, and
 276 τ_{EKE} varies between 2.5 to 4.2 days. The poor approximation at synoptic timescales suggests
 277 that at these timescales the other terms in (2) (such as momentum fluxes and EKE fluxes) indeed
 278 matter. Nonetheless, Fig. 3 shows that such a simple relationship holds reasonably well at periods
 279 longer than 10 days. This is consistent with the prediction of the multiscale asymptotic theory of
 280 Boljka and Shepherd (2018), after averaging over synoptic time and spatial scales. Similar results
 281 can be obtained also with a 10° and 90° latitudinal band (not shown), which means that the rela-
 282 tionship is robust for latitudinal averages of 10 degrees and wider. This is consistent with Wang
 283 and Nakamura (2015, 2016).

284 Note that the real and imaginary parts of the cross-spectra cross at a higher frequency than for
 285 the momentum flux convergence and zonal mean zonal wind, due to the damping timescale τ_{EKE}
 286 being significantly smaller than τ , implying stronger baroclinic damping processes compared to
 287 the barotropic ones. Consequently, the phase difference (Fig. 3a,b ii) increases more gradually
 288 than for the barotropic processes (Fig. 2b) and by frequency 0.25 cycles per day reaches just
 289 below 80° . This suggests that the quasi-steady relationship $[K_E]/\tau \approx \alpha_{EKE}[\nu^* \theta^*]$ holds down to
 290 periods of about 20 days for EKE and heat flux, whereas for momentum flux convergence and
 291 zonal mean zonal wind it only holds at periods longer than about 50 days. We thus consider the
 292 low-frequency range with periods longer than 50 days to be in a quasi-steady balance.

293 *b. Power spectra*

294 Power spectra for the model equinox configuration are calculated for the PC timeseries of EOF
295 fields (SAM, BAM, EHF and EMF) for the first two or three modes of variability in Fig. 4. The
296 frequency spectra for the tendency of SAM and BAM are also shown as these two modes show
297 mainly low frequency behavior, whereas their tendencies reflect the higher frequency behavior
298 as well. This is clearly shown in Fig. 4 where SAM1,2 and BAM2,3 show predominantly low
299 frequency behavior with the highest peaks well beyond 50 days, whereas their tendencies show
300 higher frequency behavior on synoptic timescales with continuous spectra peaked around 10 days.
301 These spectra suggest that at lower frequencies, zonal mean zonal wind and EKE are related to
302 the eddy fluxes (the lower frequency part of the EMF1,2 and EHF2,3 spectra), whereas at higher
303 frequencies it is rather their tendencies that are related to the eddy fluxes (the higher frequency
304 part of the EMF1,2 and EHF2,3 spectra), distinguishing the different behavior anticipated from
305 (4) and (6).

306 The power spectrum for BAM1 instead has a high frequency peak around a 40 day period and
307 has another peak at lower frequencies, while its tendency shows a continuous spectrum peaked
308 around a 20 day period. This suggests that the lower and higher frequency behaviors (reflected in
309 EKE and in the tendency of EKE) for BAM1 are not well separated and overlap in the frequency
310 domain, in contrast to the other modes. EHF1 and the tendency of BAM1 both show a distinct
311 peak at about the 20-30 day period, which is consistent with the results of Thompson and Barnes
312 (2014) and Wang and Nakamura (2015) who found an oscillatory behavior between EKE (or wave
313 activity) and heat flux with similar periods. The spectra suggest that this oscillatory behavior at
314 these periods is distinct.

315 From the power spectra a frequency cut-off can be determined for the high-pass and low-pass
316 filtering. The thick solid grey line in Fig. 4 shows the chosen cut-off period of 50 days, which
317 distinguishes between the distinct behavior in the two frequency bands (i.e. low pass includes
318 periods longer than 50 days and high pass includes periods shorter than 50 days). Note that the
319 cut-off period of 30 days that was used in previous studies (e.g. Sparrow et al. 2009) would not
320 be a good choice here. While the low pass data represent modes of variability in quasi-steady
321 balance, the high pass data include both synoptic timescale variability as well as intermediate
322 timescales (timescales longer than synoptic and shorter than quasi-steady balance) where both the
323 time tendency and linear damping terms in (4, 6) are non-negligible.

324 It is clear from the power spectra that higher frequencies overlap and it is hard to separate
325 the high-frequency behavior of EHF1 and BAM1 from that of EHF2,3, EMF1,2, BAM2,3 or
326 SAM1,2 from the power spectra alone. However, at low frequencies there are distinct spectral
327 peaks. Because the model set-up is statistically stationary, these spectral peaks presumably arise
328 from a limited sampling of red-noise variability. We can use this feature to our advantage, because
329 it provides a clear fingerprint of covariability when the peaks match between different quantities.
330 While the peaks themselves are not robust to subsampling (e.g. Fig. S2 in supplementary material),
331 all of the conclusions below are robust to subsampling and indeed that robustness provides more
332 confidence in the presented results.

333 The dash-dotted and dashed lines in Fig. 4 show the peaks in the SAM1 and SAM2 power
334 spectra, respectively, for periods between 50 and 1000 days. In order to be identified, the peaks
335 had to be separated by at least 10 data points (with frequency resolution of $1/9360 \text{ days}^{-1}$) and
336 had to be higher than $5/6$ of the maximum value in the low-frequency part of the spectrum. The
337 SAM1 peaks were then projected on the BAM2, EHF2 and EMF1 panels, whereas the SAM2
338 peaks were projected on the BAM1, BAM3, EHF1, EHF3 and EMF2 panels to locate matching

339 peaks. If the main peaks approximately match, then this provides prima facie evidence for a
 340 relation between the modes. For the model equinox configuration this shows a clear low-frequency
 341 relation between SAM1, EMF1, BAM2 and EHF2. The relations between SAM1 and EMF1,
 342 and between BAM2 and EHF2, reflect the quasi-steady limit of (4) and (6) (i.e. $z_u/\tau \approx m$ and
 343 $[K_E]/\tau_{EKE} \approx \alpha_{EKE}[\nu^* \theta^*]$), but the cross-relation between SAM1 and BAM2 is non-trivial. The
 344 strong positive correlation for low-pass data is shown in the top row of Table 2. Similarly, there
 345 is a different low-frequency relation between SAM2, EMF2, BAM3 and EHF3, pointing to a non-
 346 trivial relation between SAM2 and BAM3. The strong positive correlation for low-pass data is
 347 shown in the top row of Table 4. The link between any of these modes and BAM1 or EHF1 is
 348 weaker (see also top row of Table 3). Therefore, we find no evidence of a quasi-steady cross-mode
 349 relationship between SAM1 and BAM1, which was the correlation examined (using unfiltered
 350 data) by Thompson and Woodworth (2014). Note that the correlations shown in Tables 2-4 are
 351 robust to subsampling, i.e. high correlations are robustly high and small or non-robust correlations
 352 are consistently small or non-robust.

353 These power spectra and correlations thus reveal three main mechanisms:

- 354 • The Thompson and Woodworth (2014) and Thompson and Barnes (2014) picture of a rela-
 355 tionship between BAM1 and EHF1 through the oscillator model, with periods of 20-30 days
 356 (intermediate timescale);
- 357 • The classical (quasi-steady) positive baroclinic feedback picture (e.g. Robinson 2000) where
 358 the storm tracks move with the jet shifts (this feedback is possible if the eddies are absorbed
 359 at a different latitude than their source region). This is reflected in the positive correlations
 360 at low frequencies between SAM1 and BAM2/EHF2, and between SAM2 and BAM3/EHF3,
 361 and in the regressions of EKE on low frequency SAM1,2 (see next section); and

- The higher frequency (synoptic timescale) picture of transient wave-mean flow interaction (e.g. Edmon et al. 1980), in which SAM1,2, EMF1,2, BAM2,3 and EHF2,3, all show power peaking around 10 days, and there are negative correlations (at zero lag) in high-pass data between SAM1 and BAM2 (see further discussion in section 5).

5. Comparison to other model configurations and to SH observations

The results from the equinox model configuration are now compared to the summer and winter hemispheres of the solstice model configuration, as well as to the SH in ERA-Interim. This is important as the different model configurations can exhibit different variability, because of different climatologies. Fig. 5 shows the low pass zonal mean zonal wind timeseries at 10 km for the different model configurations. It is clear that the summer and equinox configurations exhibit more persistence in their jet variability compared with the winter configuration. In particular, the shifting modes (SAM1, BAM2) in these two configurations show a clear dominance over the rest of the modes (Table 1).

Fig. 6 shows the EKE and eddy heat flux cross spectrum analysis for the winter (a) and summer (b) model configurations, and for ERA-Interim (c). These, together with Fig. 3a, show the robustness of the relationship (6) between EKE and eddy heat flux for periods longer than 10 days and for an average over a few latitudinal bands. (A 10 degree average is sufficient, but the signal is stronger for a 20 degree average, hence the former was omitted for brevity.) This is consistent with the decoupling of baroclinic and barotropic modes of variability under synoptic scale averaging (as predicted by Boljka and Shepherd 2018) and is robust for all model configurations and for ERA-Interim (i.e. independent of setting), in the sense that the momentum fluxes are not needed to account for EKE variability at intermediate timescales. The EKE damping timescale τ_{EKE} varies between 1.5 and 4.2 days, while the parameter $|\alpha_{EKE}|$ varies between 5.6 and $11.4 \times 10^{-5} \text{ m K}^{-1}$

385 s^{-2} . While τ_{EKE} is consistent with the value found in Thompson et al. (2017), $|\alpha_{EKE}|$ is larger.
 386 This is because Thompson et al. (2017) regressed the tendency of EKE onto the heat flux to calcu-
 387 late $|\alpha_{EKE}|$, and the former is dominated by higher frequencies (as shown through power spectra,
 388 e.g. Fig. 4), whereas here we calculate it for periods longer than 10 days where the relationship
 389 (6) is robust, and the EKE, not its tendency, is used for calculations.

390 Figs. 7-9 show the power spectra for the winter and summer model configurations, and for
 391 ERA-Interim (with the same panels as in Fig. 4). These power spectra imply robust relationships
 392 between SAM and EMF modes, and between BAM and EHF modes, at all frequency ranges, ac-
 393 cording to (4) and (6), respectively. BAM1 and EHF1 exhibit power in the intermediate frequency
 394 range, for which the cross spectra showed a decoupling from the barotropic dynamics, whereas the
 395 rest of the modes exhibit the synoptic timescale (around 10 day periods) and quasi-steady (periods
 396 much longer than 50 days) behavior. While the links between SAM and EMF modes and between
 397 BAM and EHF modes follow from the theory presented in section 3, the links between the SAM
 398 and BAM modes are non-trivial. To elucidate these links, the correlations between different SAM
 399 and BAM modes are given in Tables 2-4, to complement the power spectra in Figs. 4, 7-9.

400 The high pass data in Tables 2 and 3 show robust negative correlations between the SAM1,2 and
 401 BAM2,1 modes, respectively. This seems broadly consistent with TEM theory. Since $\partial[u]/\partial t$ is
 402 proportional to $\nabla \cdot \mathbf{F}$ (e.g. (2.3a) in Edmon et al. 1980) and $\partial[K_E]/\partial t$ is proportional to $-\nabla \cdot \mathbf{F}$
 403 (2) (note that $[u]$ is generally westerly in the midlatitudes and hence does not affect the sign of the
 404 correlations), a negative correlation between corresponding SAM and BAM modes is expected on
 405 synoptic timescales as the tendencies reflect the high frequency behavior (as seen from the power
 406 spectra). SAM1 is a dipolar mode and thus matches BAM2. Although SAM2 is a tripolar mode
 407 and therefore might be expected to match BAM3, the correlation between SAM2 and BAM3 at
 408 high frequencies (Table 4) is non-robust or even negligible. Instead, SAM2 is seen to be negatively

409 correlated with BAM1, which projects onto the center of SAM2. These negative correlations
410 between SAM1 and BAM2 and between SAM2 and BAM1 are further confirmed in Figs. 10 and
411 11, where the regressions of high-pass EKE (shading) on high-pass SAM modes tend to exhibit
412 the opposite sign to high-pass $[u]$ (contours) regressions on the same modes.

413 The low pass data in Tables 2 and 4 show robust positive correlations between the SAM1,2
414 and BAM2,3 modes, respectively, consistent with the quasi-steady positive baroclinic feedback
415 (Robinson 2000) described in section 4b. Moreover, there is a clear correspondence between the
416 SAM1,2 and BAM2,3 low-frequency spectral peaks in all cases (Figs. 4, 7-9). Figs. 12 and 13
417 further show that the regression of low-pass EKE on low-pass SAM1 and SAM2 reflects BAM2-
418 and BAM3-like behavior, respectively, and that positive SAM modes are related to positive BAM
419 modes (i.e. positive wind anomaly is associated with positive EKE anomaly indicating a storm
420 track shift with the jet stream, a positive baroclinic feedback mechanism), consistent with the
421 correlations. Figs. S3 and S4 (supplementary material) also show that the spatial structures of the
422 SAM1,2 and BAM2,3 modes for all model configurations and for ERA-Interim are in phase, i.e.
423 the major peaks in the SAM and BAM modes closely follow each other.

424 On the other hand, the low pass correlations between SAM2 and BAM1 are non-robust (Table
425 3), and there is no clear correspondence between their low-frequency spectral peaks (Figs. 4, 7-9).
426 This implies that any link between the SAM2 and BAM1 modes is state-dependent. This is further
427 demonstrated in Fig. S4, which shows the spatial structures of the SAM2 and BAM1 modes.
428 While it is clear from this figure that the main peaks in SAM2 and BAM1 for ERA-Interim are in
429 phase and could explain the high correlation between the two modes, it is less clear for the model
430 configurations. The winter configuration shows a high correlation between SAM2 and BAM1,
431 however the spatial structures are out of phase, suggesting that the high correlation could be a

consequence of the chosen cut-off period (50 days) as in this case the BAM1 power spectrum peaks around 50 days (Fig. 7).

The correlations for the unfiltered data reflect the combination of high and low frequency behavior. This is especially true for SAM1 and BAM2 (Table 2) where the unfiltered correlations are dominated by the low frequencies, however the weaker correlations in the unfiltered case suggest the influence of the negative high frequency correlations (consistent with Sparrow et al. 2009). Fig. 14 further demonstrates this through a much lower correlation at zero lags which increases at positive and negative lags (approximately ± 5 days). Thus, the negative high-frequency correlations depress the correlations at short time lags. This behavior also explains the negative correlation between SAM1 and BAM2 for ERA-Interim at zero lag. Table 4 shows that the unfiltered correlations between SAM2 and BAM3 are dominated by low frequency behavior. In contrast, Table 3 shows that the unfiltered correlations between SAM2 and BAM1 for the equinox and summer model configurations are dominated by the high frequency behavior, whereas for the winter model configuration and ERA-Interim a combination of low and high frequency behaviour is reflected in the unfiltered correlations. Note also that SAM1 and SAM2 can exhibit significant correlations at non-zero lags, especially for the winter configuration where the separation of modes is smaller (Sheshadri and Plumb 2017; note that they used the same winter and summer model configurations as used here). Hence, the SAM1 and SAM2 modes could together represent propagating modes of variability and should not necessarily be considered separately (Sparrow et al. 2009; Sheshadri and Plumb 2017). Examining the low-frequency spectral peaks is a way to determine whether there is co-variability of SAM1 and SAM2.

6. Summary and conclusions

This study has investigated the coupling between the baroclinic (BAM) and barotropic (SAM) modes of variability using power- and cross-spectrum analyses, regressions, and correlations in different Held-Suarez model configurations and in ERA-Interim SH reanalysis.

We have shown through the cross-spectrum analysis that there is a robust relationship across timescales between EKE and eddy heat fluxes (6), analogous to that between zonal mean zonal wind and eddy momentum flux convergence (4) (Lorenz and Hartmann 2001). However, the former relationship is weaker as it fails for periods shorter than about 10 days, and the quasi-steady balance between EKE and heat flux is non-negligible at intermediate timescales (at least for periods longer than 20 days, consistent with the oscillator model of Thompson and Barnes 2014). This is a consequence of a robustly shorter damping timescale on EKE ($\tau_{EKE} \approx 3$ days) compared to the zonal mean zonal wind damping timescale ($\tau \approx 10$ days), and is reflected in the reduced curvature of the phase difference plot in Fig. 3a(ii) compared with Fig. 2b. The weaker relationship between EKE and heat flux is understandable due to the presence of additional terms in the EKE equation (2), moreover asymptotic theory (Boljka and Shepherd 2018) shows that one needs to average over the synoptic temporal and spatial scales to obtain this relationship. A stronger relationship might be possible using wave activity instead of EKE; this is left for future work.

These cross-spectra relationships suggest a proximate link between zonal mean zonal wind and eddy momentum flux only (4), and between EKE and eddy heat flux only (6), recognising that the eddies are themselves baroclinic. The latter link is consistent with a decoupling of the baroclinic (BAM) from the barotropic (SAM) modes of variability (as in Thompson and Woodworth 2014),

475 at least at periods longer than 10 days, as predicted by the asymptotic model for intermediate
476 timescales (i.e. not for quasi-steady-state).

477 The frequency power spectra of eddy momentum and heat fluxes reveal that they generally
478 exhibit a broad peak at higher frequencies (< 30 day periods), as well as distinct peaks at lower
479 frequencies (> 50 day periods). The higher frequency eddy fluxes are related to the tendencies
480 of EKE and of zonal mean zonal wind (i.e. $\partial z_u / \partial t \approx m$, $\partial [K_E] / \partial t \approx \alpha_{EKE} [v^* \theta^*]$), whereas the
481 lower frequency peaks relate to the quantities themselves (EKE or zonal mean zonal wind; i.e.
482 $z_u / \tau \approx m$, $[K_E] / \tau_{EKE} \approx \alpha_{EKE} [v^* \theta^*]$). This was indeed confirmed by the cross spectrum analysis
483 as mentioned above.

484 There is a direct quasi-steady relationship between EMF and SAM, and between EHF and BAM,
485 which applies mode by mode, as can be seen through direct matching of low-frequency peaks in
486 the power spectra and is seen in all model configurations and in ERA-Interim. There are also
487 cross-mode relationships at quasi-steady-state. There is a robust positive relation between SAM1
488 and BAM2 (shifted jet and storm track) and between SAM2 and BAM3 (strengthened jet and
489 storm track), reflecting a positive baroclinic feedback (Robinson 2000). The relationships between
490 the SAM2 and BAM1 modes are less robust and depend on model climatology and variability.
491 These relationships could be the subject of future investigations, but can be expected to be state-
492 dependent. We find no evidence of a cross-mode relationship between SAM1 and BAM1, which
493 was the correlation examined by Thompson and Woodworth (2014).

494 There are also cross-mode relationships in high pass data, which are more complex (reflecting
495 transient wave-mean flow interaction and baroclinic life cycles) and tend to be of opposite sign to
496 those at lower frequencies. Thus, combining low and high pass data leads to a confusing picture
497 as it combines different kinds of behavior that can exhibit some cancellation between them (as
498 shown by Sparrow et al. 2009).

499 In summary, this study has shown that the nature and extent of the coupling between barotropic
500 and baroclinic modes of extratropical atmospheric variability depends strongly on the timescale
501 of variability. On synoptic timescales there is negative coupling through the baroclinic life cycle
502 (Simmons and Hoskins 1978); on quasi-steady timescales (periods longer than 50 days) there is
503 positive coupling through the baroclinic feedback mechanism (Robinson 2000); and on interme-
504 diate timescales there is a decoupling, with purely baroclinic variability that can manifest itself in
505 a baroclinic oscillator (Thompson and Barnes 2014), consistent with weakly nonlinear models of
506 baroclinic instability (Pedlosky 1970). In the quasi-steady limit the pulsating modes of variability
507 and their correlations depend sensitively on the model climatology. This could have implications
508 for the modeled circulation response to climate change.

509 *Acknowledgments.* This work was funded by the European Research Council (Advanced
510 Grant ACRCC, “Understanding the atmospheric circulation response to climate change” project
511 339390). We thank the three anonymous reviewers for their comments which helped improve
512 the original manuscript. We acknowledge Nick Byrne, Aditi Sheshadri, Simon Peatman, Tom
513 Frame, Clare Watt, and Chris Smith (Met Office) for helpful discussions. The model data can be
514 reproduced using the Unified Model (details and scripts are available upon request).

515 **References**

- 516 Ambaum, M. H. P., and L. Novak, 2014: A nonlinear oscillator describing storm track variability.
517 *Quart. J. Roy. Meteor. Soc.*, **140**, 2680–2684.
- 518 Andrews, D. G., and M. E. McIntyre, 1976: Planetary waves in horizontal and vertical shear: the
519 generalized Eliassen-Palm relation and the mean zonal acceleration. *J. Atmos. Sci.*, **33**, 2031–
520 2048.

521 Bloomfield, P., 2000: *Fourier analysis of time series: an introduction*. Wiley, 286 pp.

522 Boljka, L., and T. G. Shepherd, 2018: A multiscale asymptotic theory of extratropical wave, mean-
523 flow interaction. *J. Atmos. Sci.*, in press, doi:10.1175/JAS-D-17-0307.1.

524 Byrne, N. J., T. G. Shepherd, T. Woollings, and R. A. Plumb, 2016: Annular modes and apparent
525 eddy feedbacks in the southern hemisphere. *Geophys. Res. Lett.*, **43**, 3897–3902, doi:10.1002/
526 2016GL068851.

527 Dee, D. P., and Coauthors, 2011: The ERA-Interim reanalysis: configuration and performance of
528 the data assimilation system. *Quart. J. Roy. Meteor. Soc.*, **137**, 553 – 597, doi:10.1002/qj.828.

529 Duchon, C. E., 1979: Lanczos filtering in one and two dimensions. *J. Appl. Meteor.*, **19**, 1016–
530 1022.

531 Edmon, H. J., B. J. Hoskins, and M. E. McIntyre, 1980: Eliassen-Palm cross sections for the
532 troposphere. *J. Atmos. Sci.*, **37**, 2600–2616.

533 Hartmann, D. L., and F. Lo, 1998: Wave-driven zonal flow vacillation in the Southern Hemisphere.
534 *J. Atmos. Sci.*, **55**, 1303–1315.

535 Haynes, P. H., and T. G. Shepherd, 1989: The importance of surface pressure changes in the
536 response of the atmosphere to zonally-symmetric thermal and mechanical forcing. *Quart. J.*
537 *Roy. Meteor. Soc.*, **115**, 1181–1208.

538 Held, I. M., and M. J. Suarez, 1994: A proposal for the intercomparison of the dynamical cores of
539 atmospheric general circulation models. *Bull. Amer. Meteor. Soc.*, **75**, 1825–1830.

540 Kidson, J. W., 1988: Indices of the Southern Hemisphere zonal wind. *J. Climate*, **1**, 183–194.

541 Lorenz, D. J., and D. L. Hartmann, 2001: Eddy-zonal flow feedback in the Southern Hemisphere.
 542 *J. Atmos. Sci.*, **58**, 3312–3327.

543 Pedlosky, J., 1970: Finite-amplitude baroclinic waves. *J. Atmos. Sci.*, **27**, 15–30.

544 Pfeffer, R. L., 1987: Comparison of conventional and transformed Eulerian diagnostics in the
 545 troposphere. *Quart. J. Roy. Meteor. Soc.*, **113**, 237–254.

546 Pfeffer, R. L., 1992: A study of eddy-induced fluctuations of the zonal-mean wind using conven-
 547 tional and transformed Eulerian diagnostics. *J. Atmos. Sci.*, **49**, 1036–1050.

548 Plumb, R. A., 1983: A new look at the energy cycle. *J. Atmos. Sci.*, **40**, 1669–1688.

549 Polvani, L. M., and P. J. Kushner, 2002: Tropospheric response to stratospheric perturbations in a
 550 relatively simple general circulation model. *Geophys. Res. Lett.*, **29**, 18–1–18–4.

551 Robinson, W. A., 2000: A baroclinic mechanism for the eddy feedback on the zonal index. *J.*
 552 *Atmos. Sci.*, **57**, 415–422.

553 Sheshadri, A., and R. A. Plumb, 2017: Propagating annular modes: Empirical orthogonal
 554 functions, principal oscillation patterns, and time scales. *J. Atmos. Sci.*, **74**, 1345–1361, doi:
 555 10.1175/JAS-D-16-0291.1.

556 Sheshadri, A., R. A. Plumb, and E. P. Gerber, 2015: Seasonal variability of the polar stratospheric
 557 vortex in an idealised AGCM with varying tropospheric wave forcing. *J. Atmos. Sci.*, **72**, 2248–
 558 2266.

559 Simmons, A. J., and B. J. Hoskins, 1978: The life cycles of some nonlinear baroclinic waves. *J.*
 560 *Atmos. Sci.*, **35**, 414–432.

- Sparrow, S., M. Blackburn, and J. D. Haigh, 2009: Annular variability and eddy-zonal flow interactions in a simplified atmospheric GCM. part I: characterization of high- and low-frequency behaviour. *J. Atmos. Sci.*, **66**, 3075–3094.
- Thompson, D. W. J., and E. A. Barnes, 2014: Periodic variability in the large-scale Southern Hemisphere atmospheric circulation. *Science*, **343**, 641–645.
- Thompson, D. W. J., B. R. Crow, and E. A. Barnes, 2017: Intraseasonal periodicity in the Southern Hemisphere circulation on regional spatial scales. *J. Atmos. Sci.*, **74**, 865–877, doi:10.1175/JAS-D-16-0094.1.
- Thompson, D. W. J., and J. D. Woodworth, 2014: Barotropic and baroclinic annular variability in the Southern Hemisphere. *J. Atmos. Sci.*, **71**, 1480–1493.
- Thorncroft, C. D., B. J. Hoskins, and M. E. McIntyre, 1993: Two paradigms of baroclinic-wave life-cycle behaviour. *Quart. J. Roy. Meteor. Soc.*, **119**, 17–55, doi:10.1002/qj.49711950903.
- Vallis, G. K., E. P. Gerber, P. J. Kushner, and B. A. Cash, 2004: A mechanism and simple dynamical model of the North Atlantic Oscillation and annular modes. *J. Atmos. Sci.*, **61**, 264–280.
- Walters, D., N. Wood, S. Vosper, and S. Milton, 2014: ENDGame: A new dynamical core for seamless atmospheric prediction. Tech. rep., Met Office, 30 pp.
- Wang, L., and N. Nakamura, 2015: Covariation of finite-amplitude wave activity and the zonal mean flow in the midlatitude troposphere: 1. Theory and application to the Southern Hemisphere summer. *Geophys. Res. Lett.*, **42**, 8192–8200.
- Wang, L., and N. Nakamura, 2016: Covariation of finite-amplitude wave activity and the zonal-mean flow in the midlatitude troposphere. Part II: Eddy forcing spectra and the pe-

582 riodic behavior in the Southern Hemisphere summer. *J. Atmos. Sci.*, **73**, 4731–4752, doi:
583 10.1175/JAS-D-16-0091.1.

584	LIST OF TABLES	
585	Table 1.	Variance explained (in %) for the first two SAM modes and the first three BAM
586		modes for different model configurations and for ERA-Interim under a Lanczos
587		50-day low pass filter. Note that the modes are numbered according to spatial
588		structure and not variance explained. 30
589	Table 2.	Correlation between SAM1 and BAM2 at lag 0 for different model configura-
590		tions and for ERA-Interim for unfiltered, low and high pass filtered data. Only
591		statistically significant correlations (exceeding 95% threshold) are given. . . . 31
592	Table 3.	As in Table 2, but for SAM2 and BAM1. 32
593	Table 4.	As in Table 2, but for SAM2 and BAM3. 33

594 TABLE 1. Variance explained (in %) for the first two SAM modes and the first three BAM modes for different
595 model configurations and for ERA-Interim under a Lanczos 50-day low pass filter. Note that the modes are
596 numbered according to spatial structure and not variance explained.

configuration	SAM1	SAM2	BAM1	BAM2	BAM3
equinox	84	11	19	70	6
summer	86	9	24	65	6
winter	59	31	32	42	13
ERA-Interim	59	25	38	23	14

597 TABLE 2. Correlation between SAM1 and BAM2 at lag 0 for different model configurations and for ERA-
598 Interim for unfiltered, low and high pass filtered data. Only statistically significant correlations (exceeding 95%
599 threshold) are given.

configuration	unfiltered	low pass	high pass
equinox	0.45	0.87	-0.55
summer	0.62	0.92	-0.55
winter	0.29	0.66	-0.31
ERA-Interim	-0.05	0.63	-0.28

TABLE 3. As in Table 2, but for SAM2 and BAM1.

configuration	unfiltered	low pass	high pass
equinox	-0.28		-0.53
summer	-0.34	0.07	-0.57
winter	-0.32	-0.65	-0.27
ERA-Interim	-0.31	-0.42	-0.29

TABLE 4. As in Table 2, but for SAM2 and BAM3.

configuration	unfiltered	low pass	high pass
equinox	0.30	0.81	0.03
summer	0.32	0.75	
winter	0.27	0.50	0.04
ERA-Interim	0.05	0.27	0.09

LIST OF FIGURES

600	LIST OF FIGURES	
601	Fig. 1.	Contours show regressions of zonal mean zonal wind ($[u]$) on a) SAM1 and c) SAM2 (con-
602		tour interval is 1 m s^{-1}), of EKE on e) BAM1, g) BAM2 and i) BAM3 (contour interval is 6
603		$\text{m}^2 \text{ s}^{-2}$), of momentum flux (v^*u^*) on b) EMF1 and d) EMF2 (contour interval is $3 \text{ m}^2 \text{ s}^{-2}$),
604		and of heat flux ($v^*\theta^*$) on f) EHF1, h) EHF2 and j) EHF3 (contour interval is 1 m K s^{-1}).
605		Colours show the climatologies of the regressed fields. Data are from the equinox model
606		configuration and were not filtered. 36
607	Fig. 2.	Imaginary and Real parts of cross-spectrum (a) and phase difference (b) between zonal mean
608		zonal wind (Z) and eddy momentum flux convergence (M). Data were split into 512-day
609		long segments overlapped by 256 days. Vertically averaged (full depth) momentum flux
610		convergence was regressed onto EOF1 of $[u]$ to obtain timeseries. Data are from the equinox
611		model configuration and were not filtered. Note that a similar figure can be obtained for
612		EOF2 of $[u]$ 37
613	Fig. 3.	Imaginary and Real parts of cross-spectrum (i) and phase difference (ii) between EKE (E)
614		and eddy heat flux (H) for data split into (a) 256, and (b) 512-day long segments overlapped
615		by a half-length. EKE was taken at 9000 m and heat flux was taken at 1500 m. Both were
616		averaged between 30°S and 50°S . Data are from the equinox model configuration and were
617		not filtered. 38
618	Fig. 4.	Power spectra (day^{-1}) of unfiltered PC timeseries of different fields as labelled. See text
619		for description of modes, also Fig. 1. Vertical grey dash-dotted and dashed lines indicate
620		the main peaks in SAM1 and SAM2 power spectra, respectively, and the grey solid line
621		indicates the frequency cut-off used later for filtering. Data are from the equinox model
622		configuration. 39
623	Fig. 5.	Low-pass zonal mean zonal wind ($[u]$) timeseries at 10 km for different model setups:
624		equinox (a), winter hemisphere (b), and summer hemisphere (c) model configurations. Note
625		that the summer hemisphere data were plotted as SH for easier comparison with other con-
626		figurations. 40
627	Fig. 6.	Imaginary and Real parts of cross-spectrum (i) and phase difference (ii) between unfiltered
628		EKE (E) and eddy heat flux (H) for (a) winter hemisphere, (b) summer hemisphere, (c)
629		ERA-Interim. Data were split into 256-day long segments overlapped by 128 days. EKE
630		was taken at 9000 m (300 hPa for ERA-Interim) and heat flux was taken at 1500 m (850 hPa
631		for ERA-Interim). Both were averaged between: (a) 35° and 55° , (b) 25° and 45° and (c)
632		40° and 60° latitude. 41
633	Fig. 7.	As in Fig. 4 but for the winter hemisphere model configuration. 42
634	Fig. 8.	As in Fig. 4 but for the summer hemisphere model configuration. 43
635	Fig. 9.	As in Fig. 4 but for ERA-Interim. 44
636	Fig. 10.	Regressions of high pass EKE (in shading; units: $\text{m}^2 \text{ s}^{-2}$) and high pass zonal mean zonal
637		wind (in contours; units: m s^{-1}) on high-pass SAM1 for (a) equinox, (b) winter, (c) summer
638		model configurations, and (d) ERA-Interim. The contour interval is 0.3 m s^{-1} (..., -0.3, 0,
639		0.3, 0.6, ...). The dashed lines represent negative values and solid lines represent positive
640		values. 45
641	Fig. 11.	As in Fig. 10 but for the regressions on high pass SAM2. 46

642	Fig. 12.	Regressions of low-pass EKE (in shading; units: $\text{m}^2 \text{s}^{-2}$) and low pass zonal mean zonal	
643		wind (in contours; units: m s^{-1}) on low-pass SAM1 for (a) equinox, (b) winter, (c) summer	
644		model configurations, and (d) ERA-Interim. The contour interval is 0.3 m s^{-1} (... , -0.3, 0,	
645		0.3, 0.6, ...). The dashed lines represent negative values and solid lines represent positive	
646		values.	47
647	Fig. 13.	As in Fig. 12 but for the regressions on low-pass SAM2. Note that the colourscale was	
648		adjusted to the values of EKE regression on this mode.	48
649	Fig. 14.	Lagged correlations between SAM1 and BAM2 (unfiltered) for equinox (black solid line),	
650		winter (black dashed line) and summer (red dashed line) model configurations, and ERA-	
651		Interim (red solid line).	49

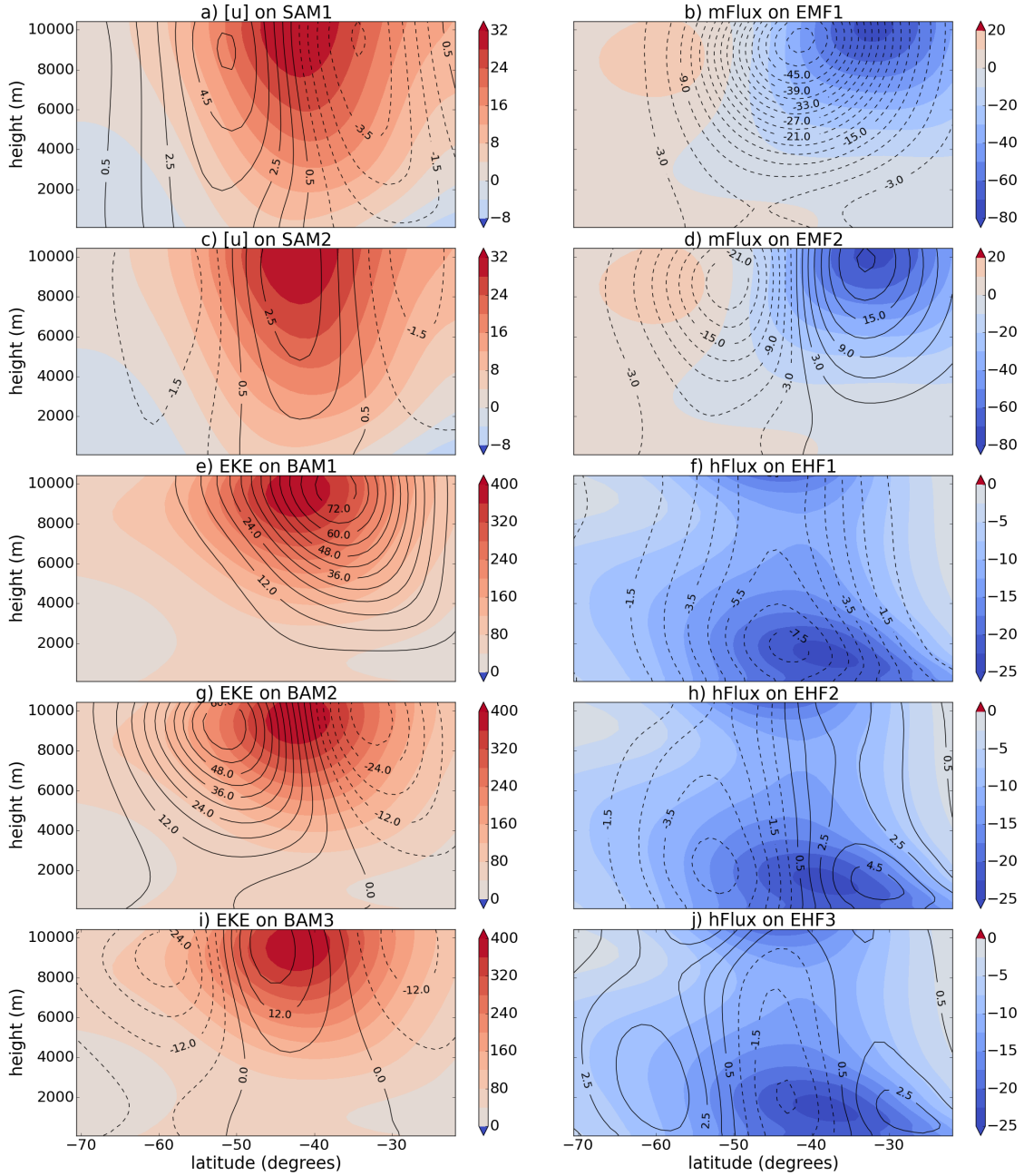


FIG. 1. Contours show regressions of zonal mean zonal wind ($[u]$) on a) SAM1 and c) SAM2 (contour interval is 1 m s^{-1}), of EKE on e) BAM1, g) BAM2 and i) BAM3 (contour interval is $6 \text{ m}^2 \text{ s}^{-2}$), of momentum flux (v^*u^*) on b) EMF1 and d) EMF2 (contour interval is $3 \text{ m}^2 \text{ s}^{-2}$), and of heat flux ($v^*\theta^*$) on f) EHF1, h) EHF2 and j) EHF3 (contour interval is 1 m K s^{-1}). Colours show the climatologies of the regressed fields. Data are from the equinox model configuration and were not filtered.

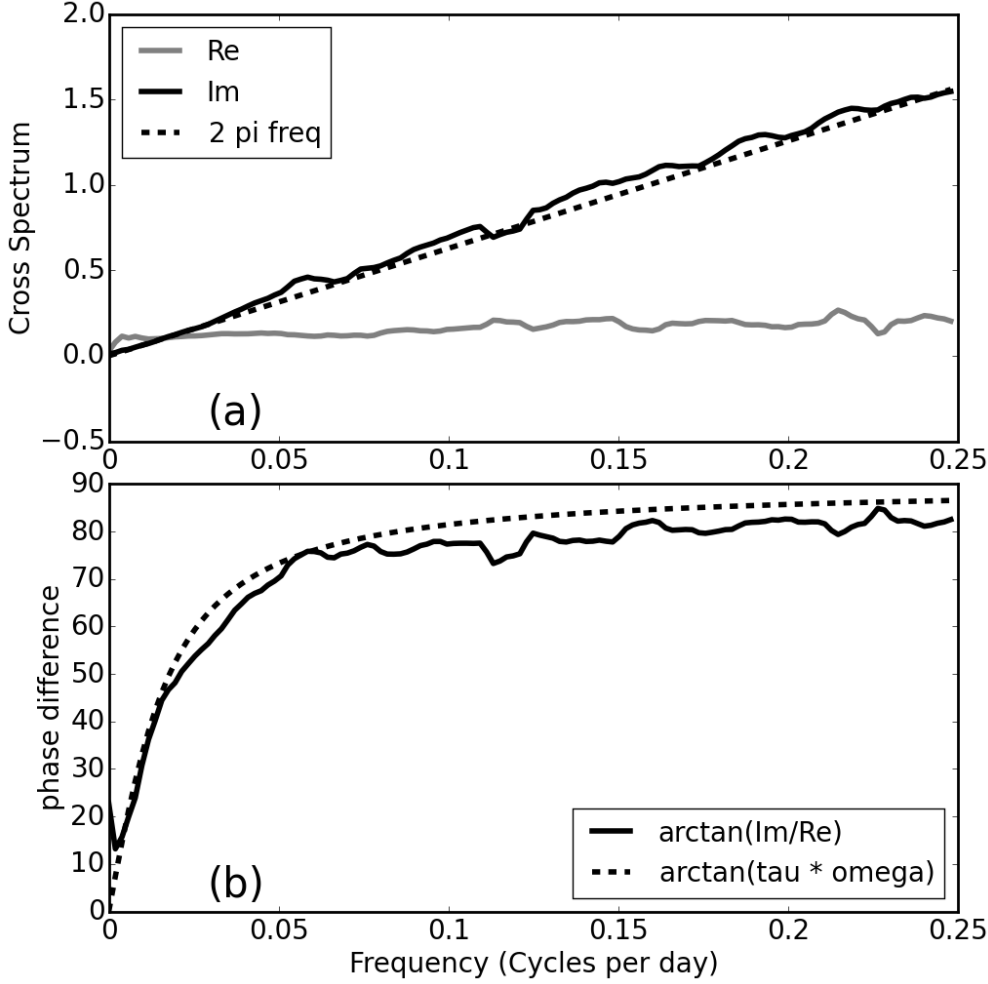


FIG. 2. Imaginary and Real parts of cross-spectrum (a) and phase difference (b) between zonal mean zonal wind (Z) and eddy momentum flux convergence (M). Data were split into 512-day long segments overlapped by 256 days. Vertically averaged (full depth) momentum flux convergence was regressed onto EOF1 of $[u]$ to obtain timeseries. Data are from the equinox model configuration and were not filtered. Note that a similar figure can be obtained for EOF2 of $[u]$.

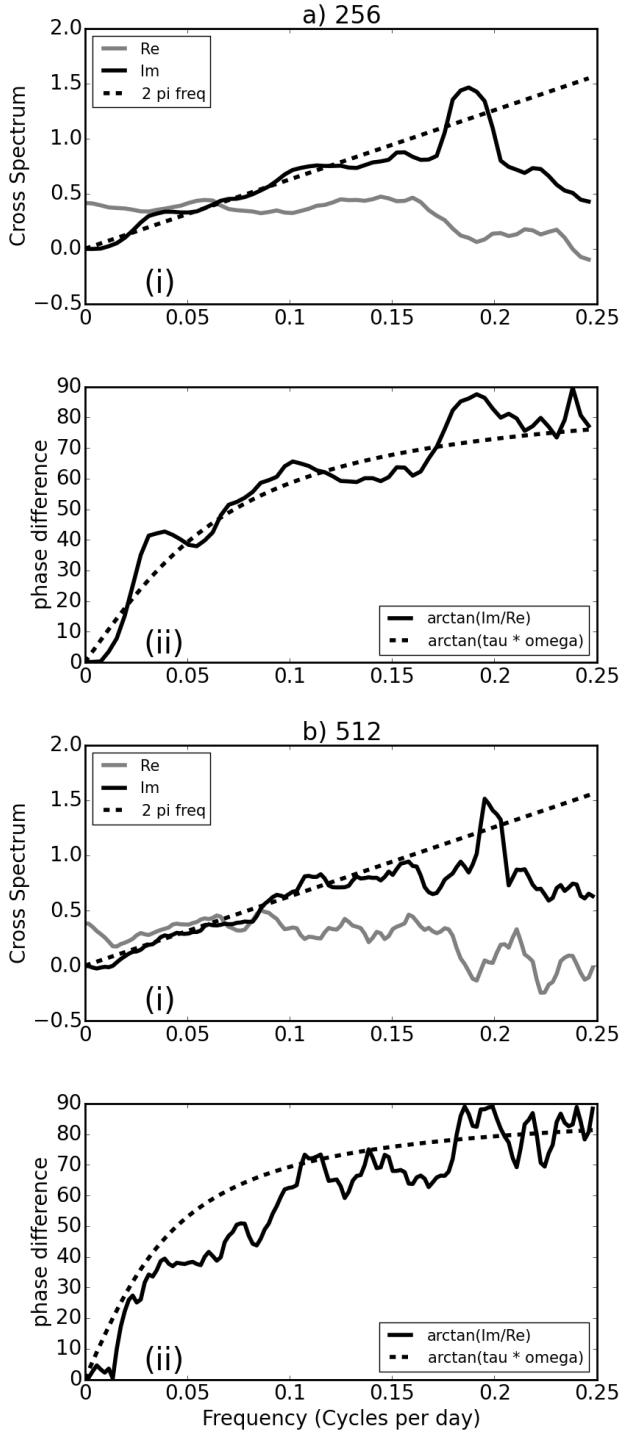


FIG. 3. Imaginary and Real parts of cross-spectrum (i) and phase difference (ii) between EKE (E) and eddy heat flux (H) for data split into (a) 256, and (b) 512-day long segments overlapped by a half-length. EKE was taken at 9000 m and heat flux was taken at 1500 m. Both were averaged between $30^\circ S$ and $50^\circ S$. Data are from the equinox model configuration and were not filtered.

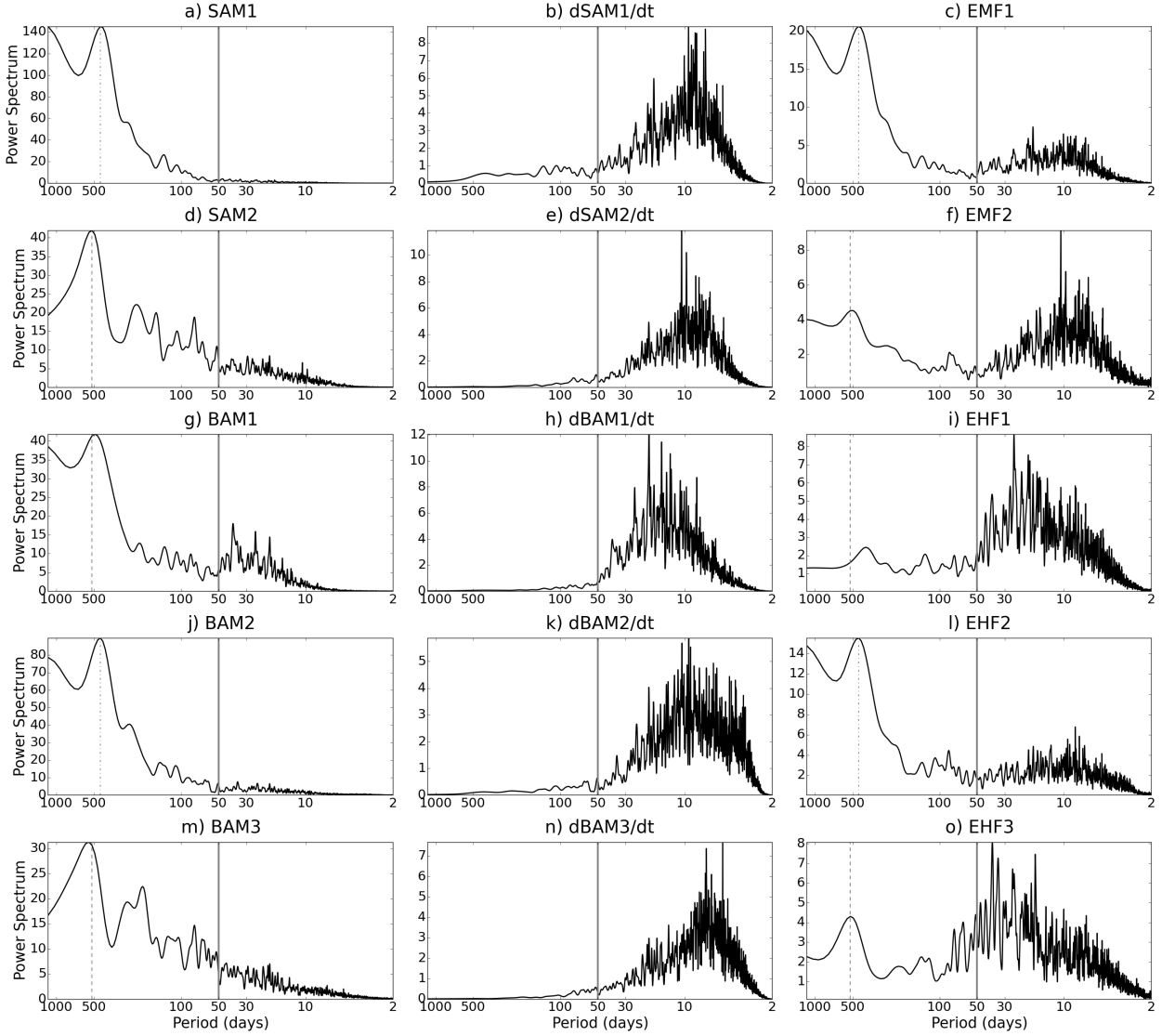


FIG. 4. Power spectra (day^{-1}) of unfiltered PC timeseries of different fields as labelled. See text for description of modes, also Fig. 1. Vertical grey dash-dotted and dashed lines indicate the main peaks in SAM1 and SAM2 power spectra, respectively, and the grey solid line indicates the frequency cut-off used later for filtering. Data are from the equinox model configuration.

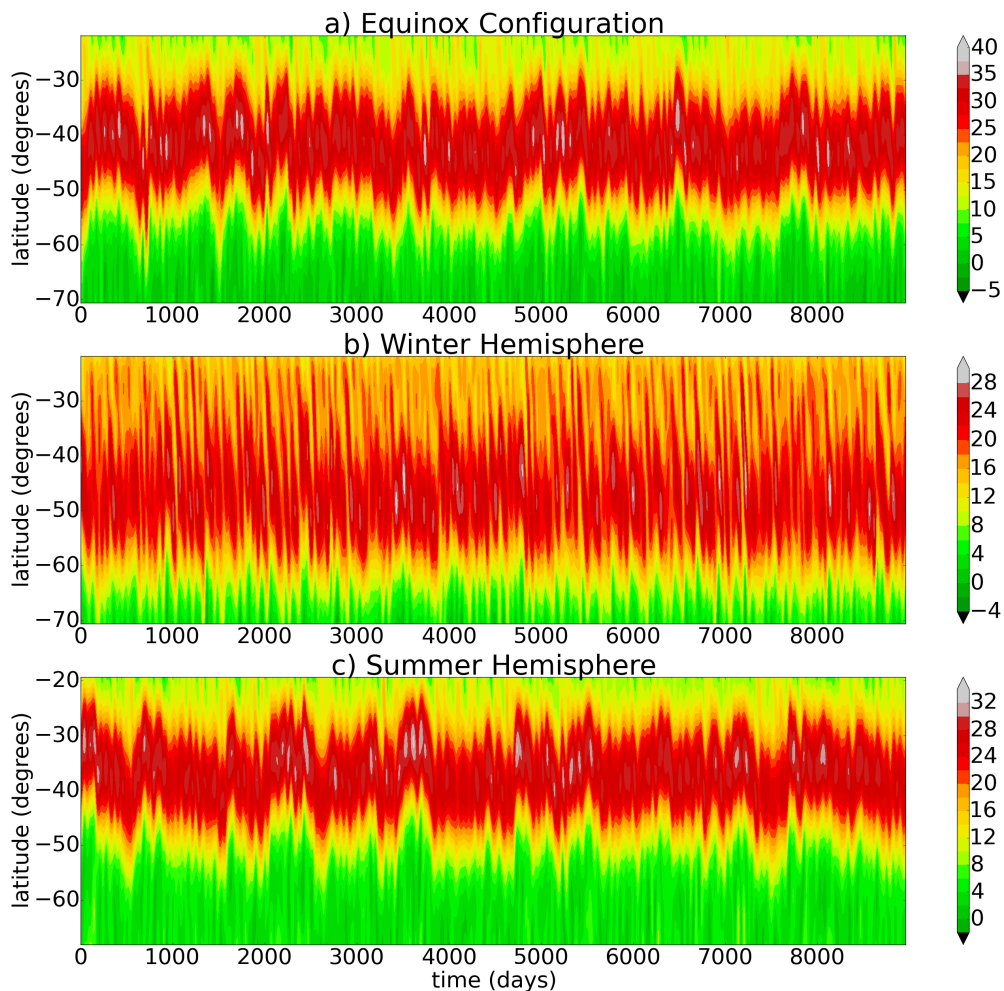


FIG. 5. Low-pass zonal mean zonal wind ($[u]$) timeseries at 10 km for different model setups: equinox (a),
 winter hemisphere (b), and summer hemisphere (c) model configurations. Note that the summer hemisphere
 data were plotted as SH for easier comparison with other configurations.

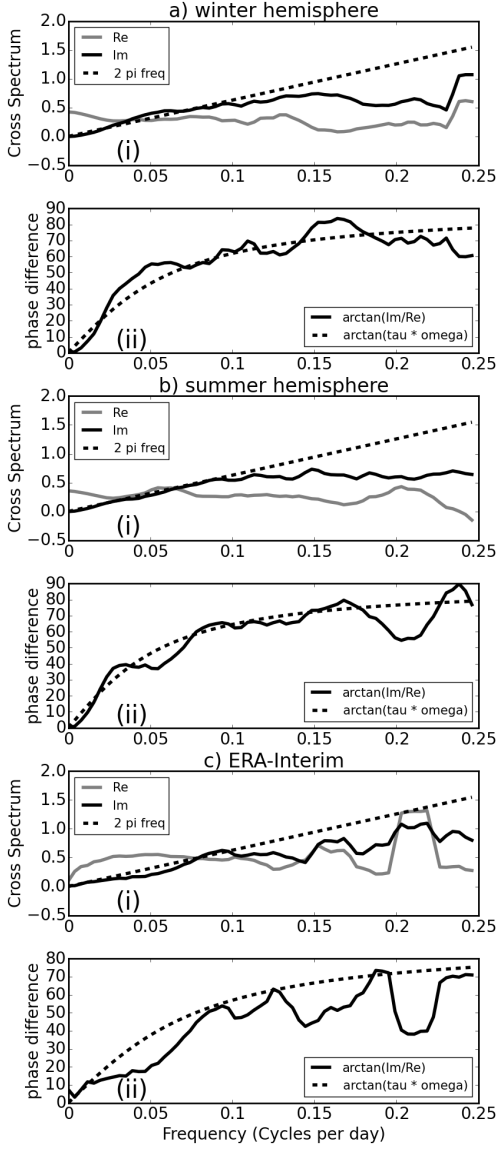


FIG. 6. Imaginary and Real parts of cross-spectrum (i) and phase difference (ii) between unfiltered EKE (E) and eddy heat flux (H) for (a) winter hemisphere, (b) summer hemisphere, (c) ERA-Interim. Data were split into 256-day long segments overlapped by 128 days. EKE was taken at 9000 m (300 hPa for ERA-Interim) and heat flux was taken at 1500 m (850 hPa for ERA-Interim). Both were averaged between: (a) 35° and 55° , (b) 25° and 45° and (c) 40° and 60° latitude.

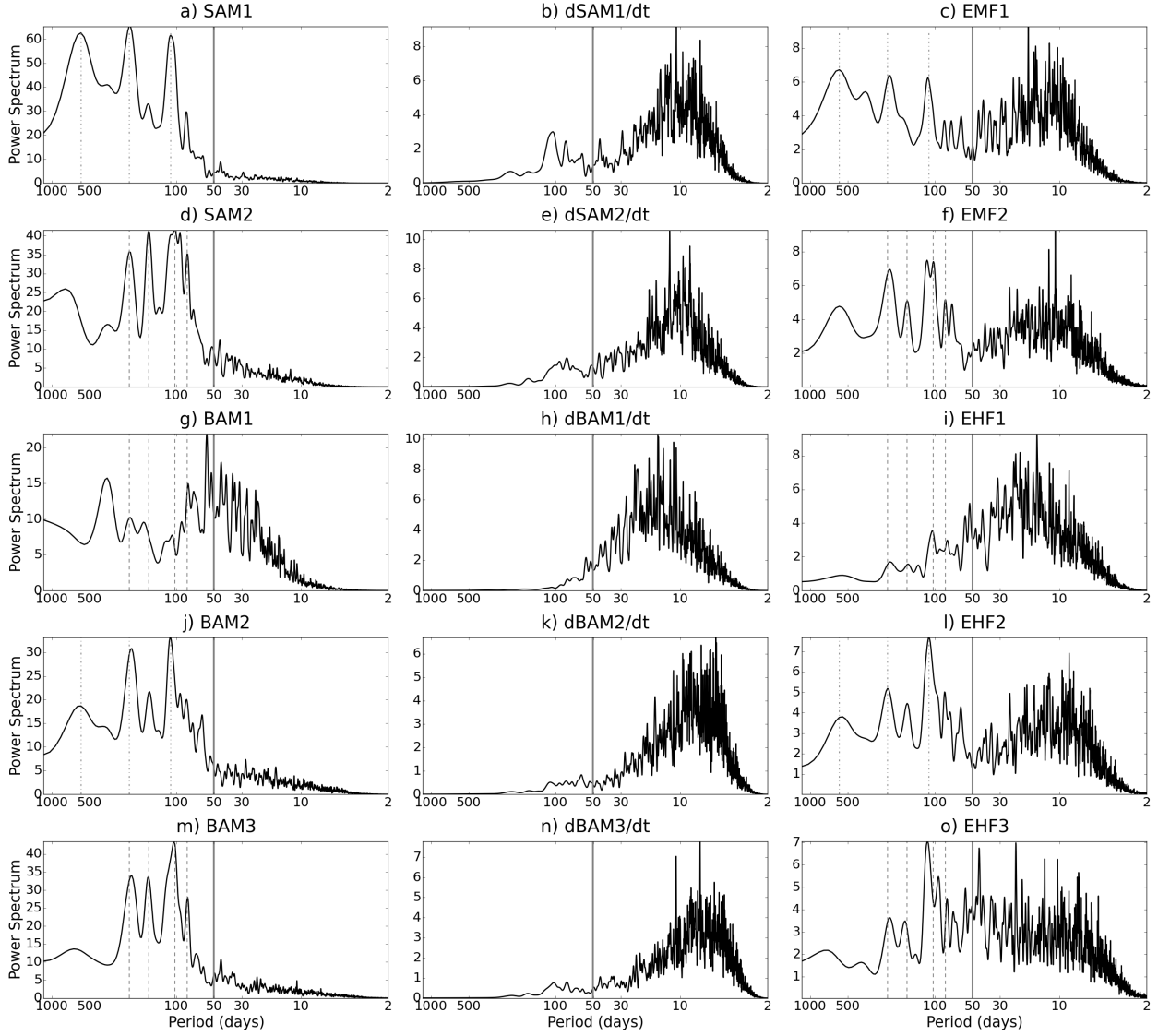


FIG. 7. As in Fig. 4 but for the winter hemisphere model configuration.

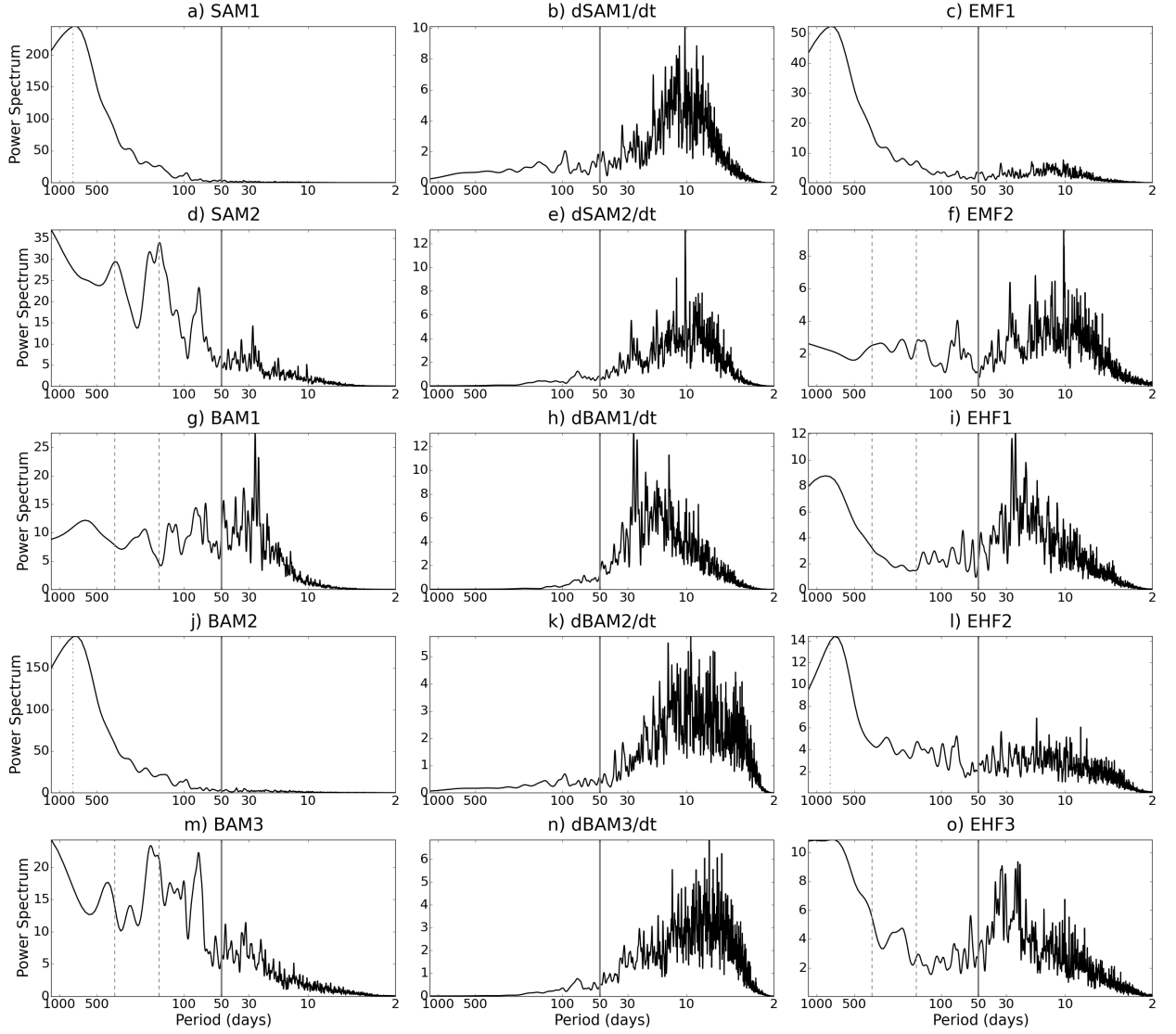


FIG. 8. As in Fig. 4 but for the summer hemisphere model configuration.

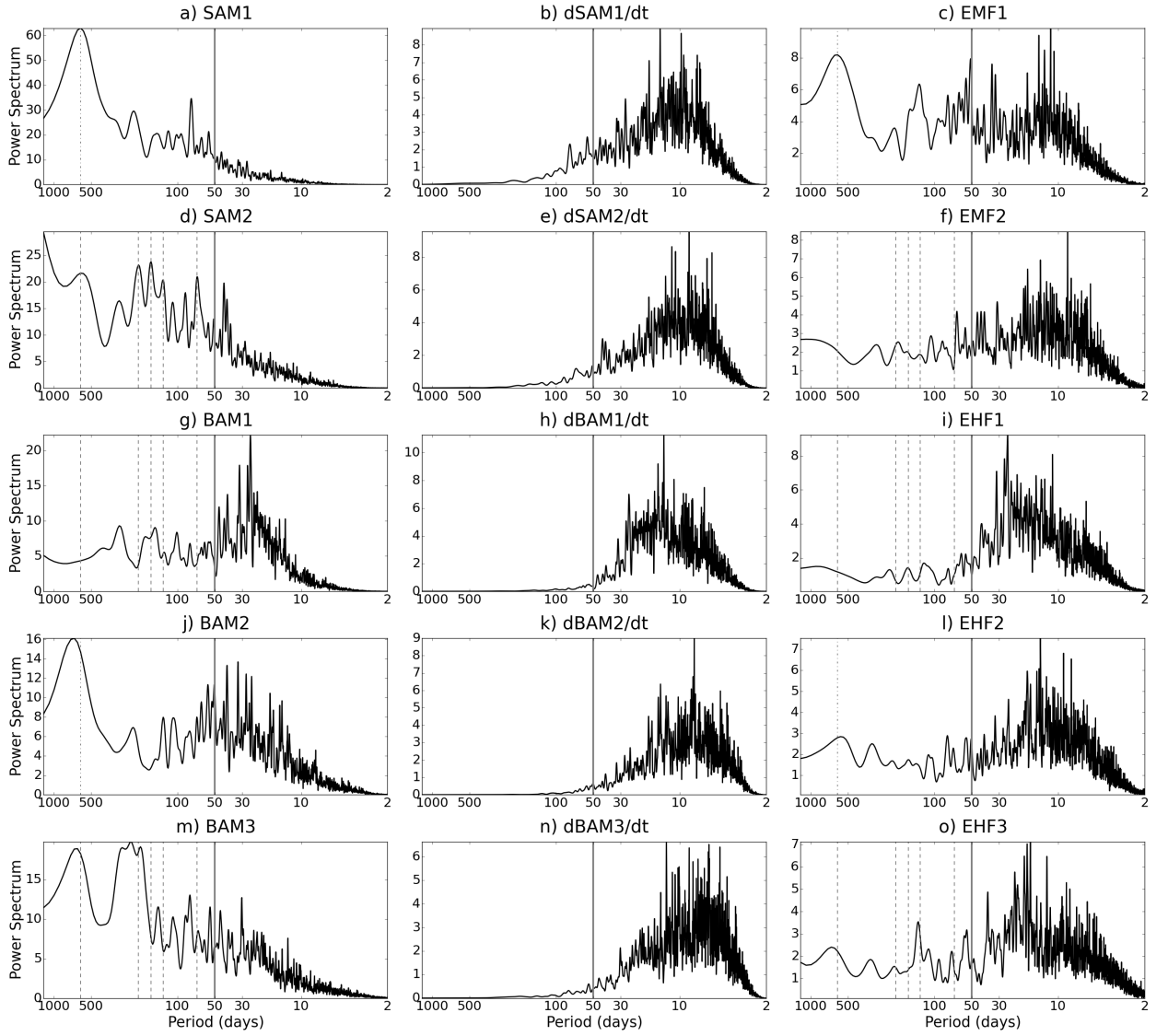


FIG. 9. As in Fig. 4 but for ERA-Interim.

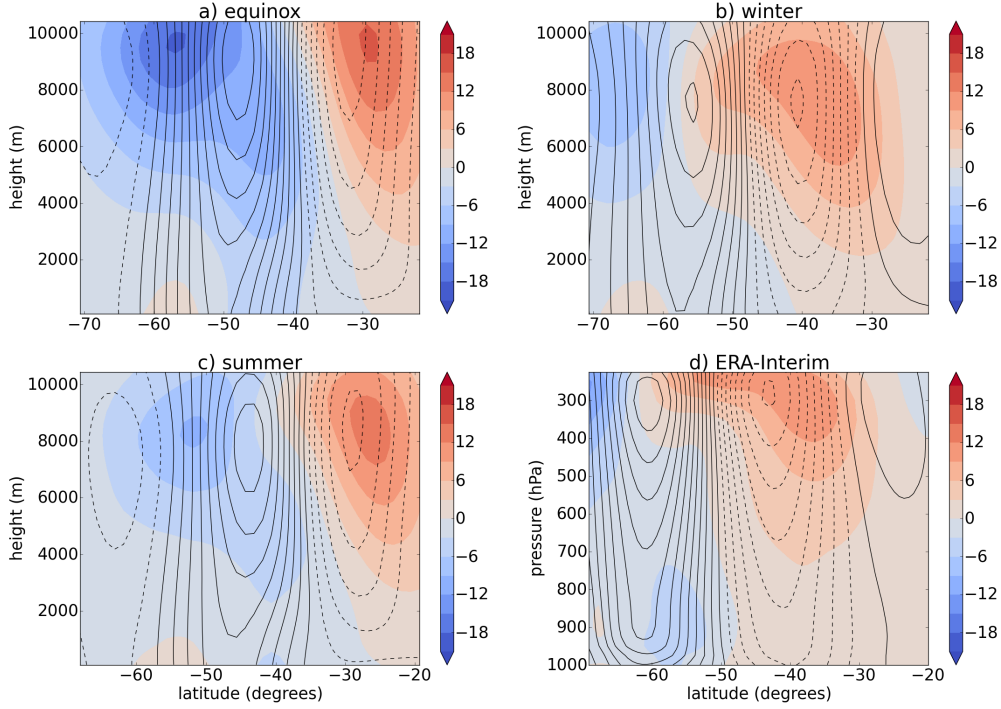


FIG. 10. Regressions of high pass EKE (in shading; units: $\text{m}^2 \text{s}^{-2}$) and high pass zonal mean zonal wind (in contours; units: m s^{-1}) on high-pass SAM1 for (a) equinox, (b) winter, (c) summer model configurations, and (d) ERA-Interim. The contour interval is 0.3 m s^{-1} (... , -0.3, 0, 0.3, 0.6, ...). The dashed lines represent negative values and solid lines represent positive values.

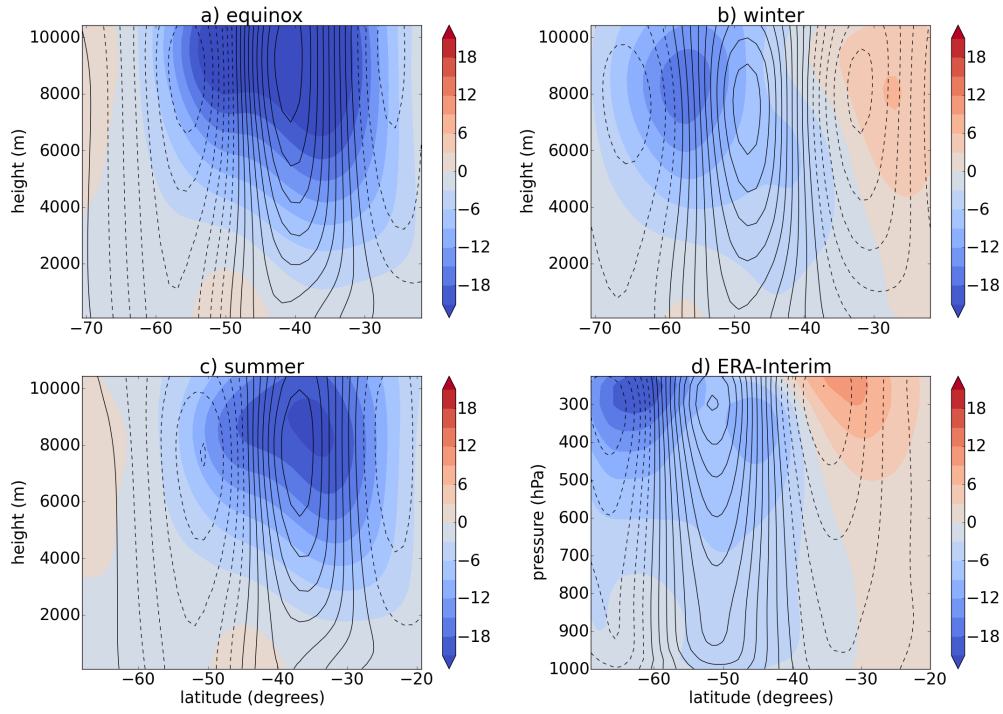


FIG. 11. As in Fig. 10 but for the regressions on high pass SAM2.

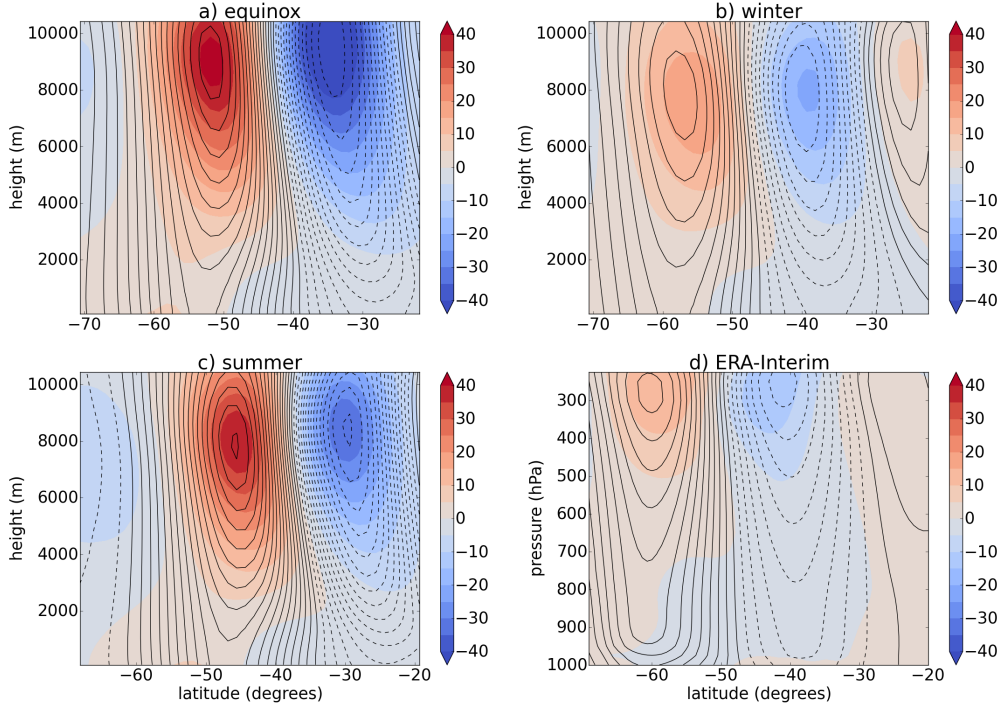


FIG. 12. Regressions of low-pass EKE (in shading; units: $\text{m}^2 \text{s}^{-2}$) and low pass zonal mean zonal wind (in contours; units: m s^{-1}) on low-pass SAM1 for (a) equinox, (b) winter, (c) summer model configurations, and (d) ERA-Interim. The contour interval is 0.3 m s^{-1} (..., -0.3, 0, 0.3, 0.6, ...). The dashed lines represent negative values and solid lines represent positive values.

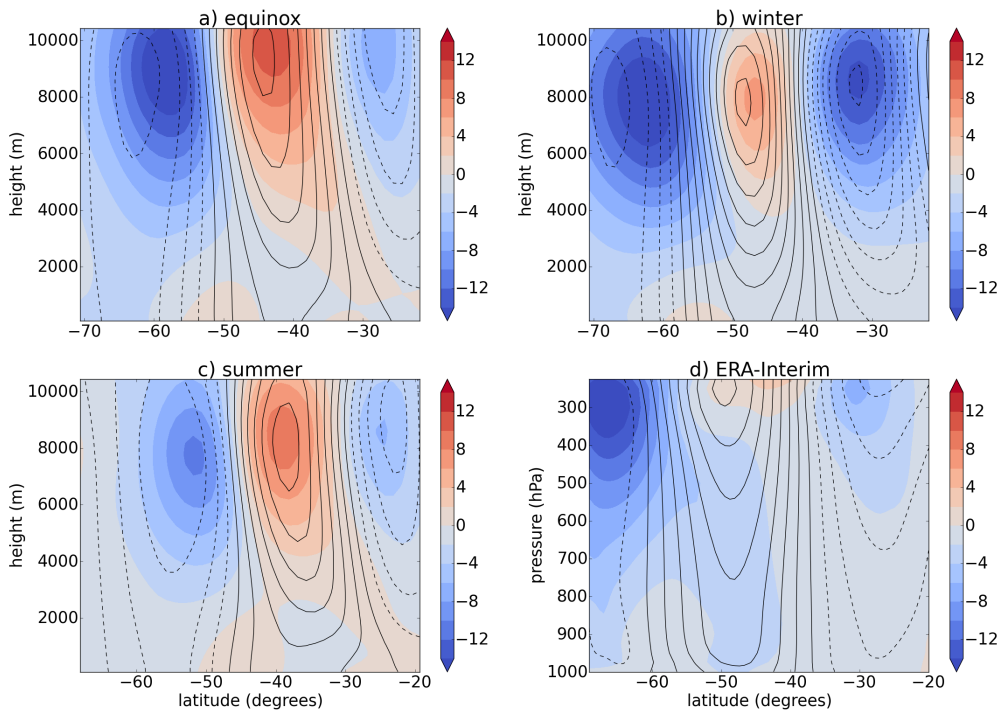


FIG. 13. As in Fig. 12 but for the regressions on low-pass SAM2. Note that the colourscale was adjusted to the values of EKE regression on this mode.

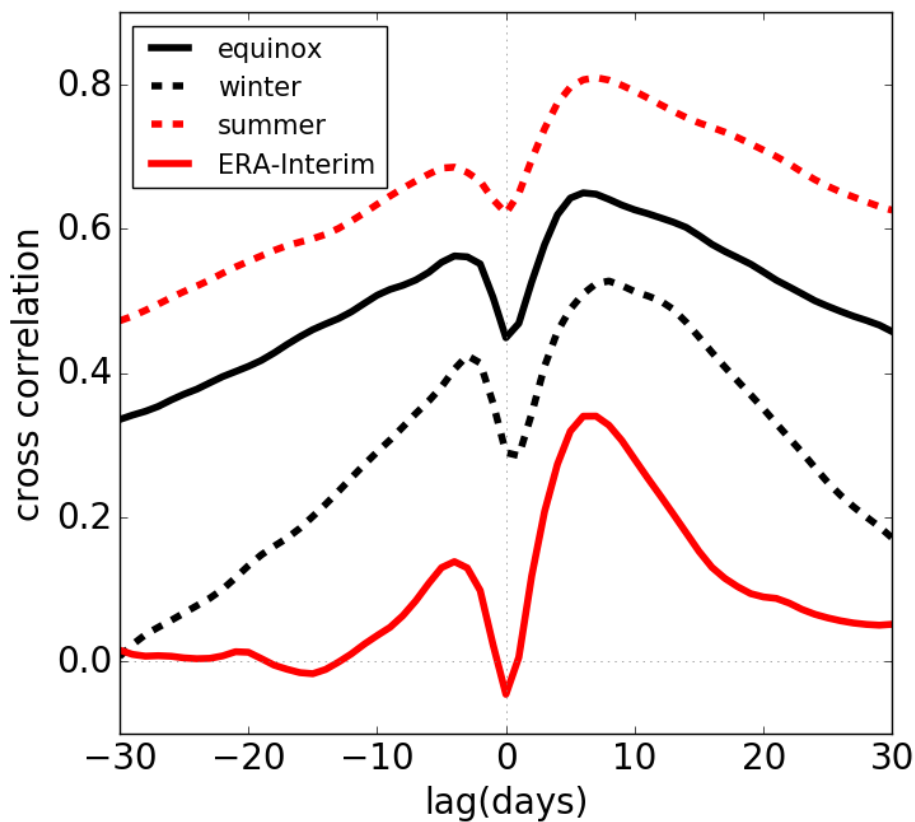


FIG. 14. Lagged correlations between SAM1 and BAM2 (unfiltered) for equinox (black solid line), winter (black dashed line) and summer (red dashed line) model configurations, and ERA-Interim (red solid line).